Research Square

Preprints are preliminary reports that have not undergone peer review.
They should not be considered conclusive, used to inform clinical practice,
or referenced by the media as validated information.

Optimization, synergistic mechanisms, and environmental safety of low-carbon cementitious materials incorporating blast-furnace slag, electrolytic manganese residue, and tailings

Ziyu Zou
zzy7767@163.com
Hunan University https://orcid.org/0009-0008-8886-8635
Zecheng Zeng
Hunan University
Mengqi Zeng
Hunan University
Zhenjun Wu
Hunan University

Research Article

Keywords: Electrolytic manganese residue, Lead–zinc mine tailings, Solid waste utilization, Mixture design, Hybrid alkali-activated cementitious materials

Posted Date: September 30th, 2026

DOI: https://doi.org/10.21203/rs.3.rs-10636420/v1

License: This work is licensed under a Creative Commons Attribution 4.0 International License. Read Full License

Abstract

Purpose

To reduce ordinary Portland cement (OPC) consumption and hazardous metallurgical waste hazards, a low-carbon cementitious binder incorporating granulated blast furnace slag (GGBS), electrolytic manganese residue (EMR), and lead-zinc mine tailings (LZMT) was developed.

Methods

A D-optimal mixture design optimized the ternary skeleton. Strong alkali activation was combined with 10% OPC to mitigate the common-ion effect. Multiscale characterizations (XRD, FTIR, TG-DTG, SEM-EDS) and standardized leaching tests were conducted to elucidate hydration mechanisms and environmental safety.

Results

The optimized system (10% OPC) achieved a 28-day compressive strength of 43 MPa with setting times of 55/115 min. Alkali activation drove LZMT to release $\mathrm{CO_3^{2-}}$, forming early monocarbonate and hydrotalcite-like phases that reconstructed into a dense (N)C-(A)-S-H gel network. Leaching concentrations of $\mathrm{Mn^{2+}}$, $\mathrm{NH_4^+}$- N, and $\mathrm{SO_4^{2-}}$ strictly complied with Class III groundwater standards (GB/T 14848 − 2017).

Conclusion

The synergistic activation strategy enables high-value, environmentally safe utilization of multi-source solid wastes for sustainable mine backfilling.

Highlight

Ternary solid wastes replace 90% OPC to produce low-carbon binders.

Alkali excitation converts inert tailings into active CO32- sources.

Mitigating the common-ion effect achieves optimal setting times.

Deeply immobilizes endogenous sulfates and reduces Mn and NH_4^+-N leaching.

1. Introduction

China aims to achieve carbon peaking and carbon neutrality to address global climate change. The building materials industry relies heavily on traditional OPC. However, OPC production causes high energy consumption and massive CO_2 emissions[1]. Moreover, a large amount of industrial solid waste, such as blast furnace slag (GGBS), electrolytic manganese slag (EMR) and lead-zinc tailings (LZMT), has accumulated in China during the processes of mining and smelting [2]. The long-term open-air storage of these solid wastes not only encroaches on the land, but the heavy metal ions (such as Mn, Pb, Zn, etc.) inside them easily pollute the soil and groundwater under leaching, which poses a serious ecological hazard[3].

In this context, exploring low-carbon cementitious materials and finding high-performance auxiliary cementitious materials to achieve cement reduction are among the research hotspots in the field of material science [4–6].Conventional solid

waste recycling practices predominantly utilize these materials as inert fillers, which often leads to significant deterioration of the mechanical properties of the cementitious system when it replaces cement. In this study, the idea of synergistic functionalization utilizing the intrinsic chemical activity of various solid wastes was proposed. For example, EMR contains a large amount of soluble sulfate (mainly gypsum)[7], which has a natural advantage as an endogenous excitation component [8]. In an alkaline excitation environment, the sulfate released by EMR can act as an efficient sulfate activator[9]. This mechanism can effectively break the structural barrier of the mineral powder glass, induce the formation of the early-stage ettringite (AFt) microcrystalline skeleton, and form a network with the C-(A)-S-H gel, thereby significantly compensating for the early strength of the system[10]. In addition, the dense hydration network can effectively seal the heavy metal ions derived from EMR through physical plugging and chemical adsorption and achieve deep solidification and stability of various harmful heavy metals, such as Mn and Pb[11, 12], which improves the environmental safety of the material[13].

Moreover, the high value-added utilization of lead-zinc tailings (LZMTs) is also an industry problem. Currently, tailings are typically used merely as inert aggregates for mine backfilling, and this conventional practice completely ignores their intrinsic resource value [14, 15]. Although LZMT is often mistaken for an absolute inert aggregate, its mineral phase is usually rich in carbonates, such as calcite[2]. In the modern supplementary cementitious material (SCM) theory, fine powder tailings can not only provide a microaggregate filling effect but also serve as heterogeneous nucleation sites to reduce the hydration energy barrier and accelerate the reaction kinetics [1, 16]. Moreover, the introduction of carbonate components can further synergistically optimize the microstructure of the composite cementitious system [17]. In a strong alkali and aluminum-rich environment, CO_3^{2-} on the surface can strongly cross-react with the active aluminum-oxygen tetrahedron released by GGBS to form monocarbonate calcium aluminate (Mc) and other carboaluminates or hydrotalcite-like compounds[18–20].

On the basis of the above theory, in this paper, a low-carbon cementitious material incorporating GGBS, EMR, and LZMT is constructed. We propose a synergistic functionalization strategy to challenge the traditional practice. The aim is to use the endogenous sulfur excitation of EMR, the physical filling/CO32- synergy of LZMT and the high activity of GGBS to realize the deep complementarity of multicomponent solid waste at the chemical and physical levels. In this study, on the basis of the D-optimal mixture design, the skeleton ratio is globally optimized, and the effects of alkali excitation parameters and cement reduction on the rheological and mechanical strength of the system are systematically explored. XRD, FTIR, TG-DTG and SEM were subsequently used to analyze the formation kinetics of early Monocarbonate (Mc) and other carboaluminate or hydrotalcite-like phases, as well as the microscopic densification characteristics of the matrix. The purpose of this study is to clarify the synergistic solidification mechanism of multisource solid waste. This provides a theoretical basis for utilizing multi-component solid wastes to prepare green low-clinker cementitious materials, indicating its potential for sustainable mine backfilling.

2. Experimental materials and analysis methods

2.1 Experimental materials

EMR and LZMT were sourced from an electrolytic manganese residue yard in Huayuan County, Hunan Province. Ordinary Portland cement (P·O 42.5) and S75 GGBS were purchased from local markets. All reagents were analytically pure, and tap water was used.

The 28-day activity index of GGBS was determined to be 74.8% in accordance with the Chinese standard GB/T 18046 – 2017. X-ray fluorescence (XRF) determined the raw material chemical compositions (Table 1). The appearance of EMR, LZMT, and GGBS is shown in Fig. 1.EMR mainly contains SO_3, CaO, SiO_2, and Al_2O_3. LZMT primarily contains CaO and CO_2. X-ray diffraction (XRD) confirmed these compositions (Fig. 2).

Scanning electron microscopy (SEM) was used to observe the raw material microstructures (Fig. 1). The EMR contains columnar, needle-like crystals and flocculent aggregates (Fig. 1a–c). This morphology aligns with its rich crystalline sulfate content (e.g., gypsum). Milled LZMT particles (Fig. 1d–f) exhibited irregular polygonal shapes and dense cleavage surfaces. This indicates that brittle fracture is typical of carbonate minerals such as calcite. GGBS (Fig. 1g–i) featured dense, irregular glassy particles with shell-like fractures. This amorphous structure enables the release of active silicon and aluminum under alkali excitation.

Cement provides an initial alkaline environment and acts as a reactant. SO_4^{2-} released from EMR stimulates GGBS activity, increasing system strength. Previous studies have shown that sulfate activators increase the strength of slag-based materials. This confirms that EMR is a feasible endogenous sulfate source. GGBS provides abundant calcium and silicon because of its latent hydraulic activity.

The LZMT contains 54.95% CaO (XRF results). XRD (Fig. 2) confirms that this calcium exists as stable crystalline calcite and dolomite. Most calcium in the tailings is chemically bound within stable carbonate lattices. Milled LZMT particles are micron-sized and comparable to GGBS and cement. This fine powder influences the slurry rheology and matrix packing density. Under alkaline conditions, calcium carbonate reacts with reactive alumina to form carboaluminates and hydrotalcite-like compounds[18, 20]. These particles also act as heterogeneous nucleation sites, accelerating cement and GGBS hydration[1, 18, 20–23]. Milled LZMT serves as a functional component in this ternary system.

Table 1
Chemical composition of the raw materials

Oxide	Mass Fraction (%)							
	SiO_2	CaO	Al_2O_3	Fe_2O_3	MgO	MnO	SO_3	CO_2
EMR	28.72	10.27	9.47	5.95	4.11	2.12	27.95	/
LZMT	3.55	54.95	2.2	0.9	8.97	/	/	26.94
GGBS	29.28	42.08	14.25	1.85	6.44	/	3.43	/
CEMENT	18.83	67.77	4.61	4.32	1.39	/	1.05	/

2.2 Pretreatment of experimental materials

Raw EMR contains a high amount of soluble NH_4^+. During strong alkaline activation, it easily volatilizes into ammonia gas, which severely deteriorates the pore structure of the hardened matrix. To resolve this, an alkaline deammoniation pretreatment was employed. Specifically, 4% NaOH was mixed with the EMR at 25°C. The *L/S* (liquid-to-solid) ratio was adjusted to 1.5 using water. After 2 h of continuous stirring, the treated EMR was dried to a constant weight at 180°C and pulverized by ball milling. Kjeldahl analysis confirmed the treatment efficacy. The total nitrogen content in the EMR significantly decreased from 3381 mg/kg to 780 mg/kg after pretreatment.

2.3 Mixture ratio and preparation

The cement content was fixed at 20% to provide initial alkalinity and early strength. The remaining 80% comprised the ternary solid waste blend. Based on preliminary tests and literature[24–26], the EMR and LZMT fractions were identically constrained between 5% and 25%. EMR below 5% provides insufficient sulfate for phase reconstruction. EMR above 25% introduces excessive soluble Mn2 + and inert particles, deteriorating strength. The LZMT range mirrored EMR to eliminate statistical bias. Consequently, GGBS was mathematically constrained between 50% and 70% to supply adequate active calcium and aluminum.

A D-optimal mixture design was used to construct the experimental plan (Fig. 3, Table 2). Mortar blocks (40 × 40 × 160 mm) were prepared per GB/T 17671–2021 for compressive strength tests. The binder-to-sand mass ratio was 1:3, and the water-to-binder ratio was 0.5. Samples were standard-cured (20 ± 2°C, RH ≥ 95%) for 24 h, demolded, and cured until testing. Paste samples were prepared identically but without sand. These were used to evaluate fluidity, setting time, and microscopic mechanisms. Paste fragments were soaked in anhydrous ethanol to arrest hydration, dried at 40°C, and ground for analysis.

Table 2
Raw material ratio of the composite cementitious materials

Sample	Mass Fraction (%)			
	CEMENT	GGBS/*A*	EMR/*B*	LZMT/*C*
1	20	50.00	5.00	25.00
2	20	50.00	25.00	5.00
3	20	70.00	5.00	5.00
4	20	53.34	8.33	18.33
5	20	56.66	11.67	11.67
6	20	53.34	13.33	13.33
7	20	63.34	8.33	8.33
8	20	50.00	5.00	25.00
9	20	50.00	25.00	5.00
10	20	60.00	5.00	15.00
11	20	53.34	18.33	8.33
12	20	60.00	15.00	5.00
13	20	60.00	15.00	5.00
14	20	58.34	8.33	13.33
15	20	50.00	15.00	15.00
16	20	50.00	20.00	10.00
17	20	70.00	5.00	5.00
18	20	58.34	13.33	8.33
19	20	50.00	10.00	20.00
20	20	60.00	15.00	5.00
21	20	50.00	15.00	15.00

2.4 Experimental methods

Macroscopic performance tests: Compressive strength, fluidity, and setting time were evaluated according to Chinese standards GB/T 17671 – 2021, GB/T 8077 – 2023, and GB/T 1346–2024, respectively. Compressive strength and fluidity were tested at a fixed water-to-binder (W/B) ratio of 0.5. Setting time was evaluated at standard consistency, with timing commencing upon liquid-powder contact. All tests report the average values of three parallel samples.

3 Results and discussion

3.1 Multisolid waste collaborative response surface optimization and strength evolution model

The compressive strength of each group of mortar is shown in Fig. 4.

A special cubic prediction model was developed using the GGBS (*A*), EMR (*B*), and LZMT (*C*) contents as independent variables and the 28 d compressive strength *(Y*) as the response value (Formula 1):

$$Y = 34.7592A + 11.7109B - 85.0687C + 9.28AB + 167.73AC - 743.26BC + 2505ABC \quad (1)$$

The ANOVA results (Table 4) indicate that the model is highly significant ($P < 0.0001$). The lack of fit is insignificant ($P = 0.1973$). The determination coefficients ($R^2 = 0.9770$, $R^2_{Adj} = 0.9672$, $R^2_{Pre} = 0.9434$) confirm excellent fitting and prediction reliability.

Table 4
Significance test of the special cubic model

Source	*F* value	*P* value	
Model	99.26	< 0.0001	significant
Liner mixture	60.17	< 0.0001	
AB	20.56	0.0005	
AC	49.62	< 0.0001	
BC	270.26	< 0.0001	
ABC	4.77	0.0464	
Lack of Fit	2.06	0.1973	Not significant

The regression equation reveals a transition from binary antagonism to ternary synergy. GGBS positively synergizes with LZMT (*AC*, + 167.73) and EMR (*AB*, + 9.28). LZMT provides heterogeneous nucleation sites. Endogenous sulfates in EMR chemically excite GGBS. Conversely, the combination of EMR and LZMT exhibits a severe antagonistic effect (*BC*, -743.26; $P < 0.0001$). Mixing these two components directly dilutes the system. It lacks sufficient active silicon and aluminum to form a continuous gel network.

However, the ternary interaction demonstrates a significant positive synergy (*ABC*, + 2505; $P = 0.0464$). When all three solid wastes coexist, their individual functions complement each other. EMR provides early chemical excitation. LZMT acts as a physical microaggregate to densify the matrix. GGBS supplies the necessary active components to construct the structural gel network.

Based on the regression model, the optimal ternary skeleton ratio was determined as 55.76% GGBS, 12.76% EMR, and 11.48% LZMT. Under this formulation, the model predicted a 28 d compressive strength of 32.08 MPa. The actual experimental strength was 31.30 MPa. The relative error between the predicted and experimental values was 2.43%. This result directly validates the accuracy of the established mathematical model.

1. **Effects of alkali excitation environment regulation on macroscopic physical and mechanical properties, setting time and fluidity**

Although the optimal ternary solid waste skeleton ratio (Ref group) was established on the basis of the response surface method, the self-hydration reaction kinetics of the system were still limited because of the relatively stable initial crystal structures of LZMT and EMR. Therefore, this study constructed a hybrid alkali excitation environment. This aims to accelerate the depolymerization of the silicon-aluminum-oxygen glass network in GGBS and promote the interface dissolution of the tailings and manganese slag.

First, the effects of the alkali activator type and equivalent on the macroscopic properties of the system were systematically explored. Two series of composite activators were prepared: Na_2CO_3 + Na_2SiO_3 (NC series) and NaOH + Na_2SiO_3 (NH series). The silicate modulus (Ms) of the activators was fixed at 1.5. Meanwhile, the total alkali equivalent (Na_2O%) was set as a distinct variable, incrementally increasing from 1% to 5%. A reference group (Ref) without any activator was also tested for comparison. It should be noted that the composite alkali activator was treated as an external admixture. Its mass was strictly excluded from the constant 450 g dry-base precursor (GGBS + EMR + LZMT + cement). During the preparation of each group of slurries, the water contained in the water glass solution was deducted to maintain a constant water-to-binder ratio of 0.5.

The system fluidity initially increased but then decreased with increasing activator concentration (Fig. 5b). The Ref group exhibited flocculation, trapping free water and resulting in a 60 mm spread. Alkali addition increased the repulsive forces of the zeta potential, thus releasing trapped water and improving fluidity [27, 28]. However, higher Na_2O% reduced fluidity. In the Na_2CO_3 + Na_2SiO_3 system, rigid precipitates form early, consuming free water and causing fluidity loss[29]. In the NaOH + Na_2SiO_3 system, extreme OH^- concentrations (Na_2O% ≥ 5%) caused flash setting.

The compressive strength trends align with the rheological behaviors (Fig. 5a). All the Na_2CO_3 + Na_2SiO_3 groups and low-concentration NaOH + Na_2SiO_3 groups (NH-1 and NH-2) yielded lower strengths than the Ref group did. For the former, CO_3^{2-} formed noncementitious carbonate precipitates with Ca^{2+}, depriving the (N)C-(A)-S-H skeleton of calcium[30]. With respect to the latter, low alkalinity failed to depolymerize the slag;[31] additionally, liquid-phase OH^- induced a common-ion effect. This reduced the solubility of calcium-rich phases, inhibiting cement hydration[32, 33].

Figure 5 (a) Effect of the type/content of the alkali activator on the compressive strength; (b) effect of the type/content of the alkali activator on expansion. Error bars represent the standard deviation of three parallel samples.

Increasing the alkali equivalent to 4% (NH-4) accelerated GGBS depolymerization. This increased the strength by 60% compared with that of NH-3 at 3 d. While NH-5 achieved the highest strength, the strength gain diminished. Excessive OH^- caused rapid settling, deteriorated workability and the introduction of structural defects. Therefore, NH-4 was selected as the optimal activator group.

To mitigate the common-ion effect, the influence of the cement content on the NH-4 system was evaluated. The reduced cement mass was proportionally distributed to the solid waste components on the basis of the optimal ternary ratio. Decreasing the amount of cement from 20% to 0% caused the strength to first increase but then decrease (Fig. 6a). At 10% cement (NH-4-2), the 28 d strength peaked at 43 MPa. At 0% cement, the strength decreased to 36.15 MPa. The setting time correlated negatively with the cement content[34] (Fig. 6b): Reducing the cement content from 20% to 0% extended the initial setting time from 40 to 80 min and the final setting time from 80 to 162 min. Notably, despite this step-wise reduction of OPC, the standard consistency water-to-binder ratio for all experimental groups remained remarkably stable at approximately 0.35, which indicates that the observed extension of setting times is purely governed by the internal hydration reactions and ion dissolution behavior.

Microscopically, 20% of the cement rapidly releases Ca^{2+} and heat in a strongly alkaline environment. Ca^{2+} reacts with $[SiO_4]^{4-}$ to form early (N)C-(A)-S-H gels, shortening the setting time[35, 36]. However, excess Ca^{2+} and OH^- alter the equilibrium. This inhibits later GGBS and EMR depolymerization. The rapidly formed hydration shell blocks ion diffusion, stunting later strength development[36–38]. Reducing the amount of cement to 10% delays initial Ca^{2+} release. This

creates an optimal engineering operation window (55/115 min setting times). It breaks the common-ion effect barrier, enabling efficient network polycondensations. Complete cement removal eliminates early nucleation sites, reducing strength. Thus, 10% cement (NH-4-2) provides the optimal balance.

3.3 Phase evolution law of the cementitious matrix of the hydration products

XRD was used to analyze the phase compositions of the Ref and NH-4-2 groups at different ages (Fig. 7). Both groups contained inert quartz and calcite from LZMT and EMR. The Ref group exhibited clear AFt (ettringite) peaks at all ages. These peaks were absent in the NH-4-2 group. Instead, NH-4-2 showed signals characteristic of monocarbonate (Mc) or hydrotalcite-like (Ht) solid solutions ($2\theta \approx 11.67°$) at 7 d. This peak did not overlap with those of gypsum. In terms of kinetics, the gypsum concentration should decrease over time, but this peak evolved differently. The secondary gypsum peak (20.7°) was also missing. To definitively rule out gypsum interference, FTIR analysis was conducted on the NH-4-2 group (Fig. 9). It confirmed enhanced CO_3^{2-} vibrations (1433 cm^{-1}) without abnormal SO_4^{2-} signals.

To track phase evolution accurately without amorphous interference, the XRD internal standard method was employed [39]. In the Ref group, the calcite/quartz intensity ratio remained constant (Fig. 8). This finding indicates that LZMT acted solely as a physical filler. EMR released SO_4^{2-}, promoting AFt formation. As hydration progressed, the AFt decomposed. Normally, this decomposition results in the formation of monosulfoaluminate (AFm-S). However, the highly polymerized (N)C-(A)-S-H gel directly absorbed the released SO_4^{2-} into its amorphous structure rather than crystallizing it [40].

In the NH-4-2 group, the calcite/quartz ratio decreased from 2.276 (3 d) to 1.881 (28 d). The activator contained no exogenous carbon. This confirms that LZMT is chemically dissolved in strongly alkaline solution. LZMT transitioned from an inert filler into a CO_3^{2-} sustained-release source. The dissolved CO_3^{2-} reacted with Ca^{2+}, $Al(OH)_4^-$, and Mg to form metastable Mc or Ht phases at 7 d. Subsequently, soluble $[SiO_4]^{4-}$ cross-linked to form a dense amorphous gel. This rapid gelation consumed effective calcium and aluminum sources. Consequently, the early-formed metastable phases disintegrated and were reconstructed. CO_3^{2-} was irreversibly sealed within the 3D (N)C-(A)-S-H network. Furthermore, strongly alkaline conditions (pH > 13) thermodynamically and kinetically inhibited AFt formation[1, 41–43].

FTIR spectra of the NH-4-2 group (Fig. 9) further revealed the polymerization characteristics of the gel network. The asymmetric stretching vibration of Si-O-T (T = Si, Al) shifted from 997 cm^{-1} (3 d) to 1010.5 cm^{-1} (7 d, 28 d). This confirms that high alkalinity drove deep polycondensations. The gel transformed from short chains into a 3D cross-linked structure. The characteristic CO_3^{2-} bands (1433, 876 cm^{-1}) increased from 3 d to 7 d but then decreased. In local microenvironments rich in Al and Mg, free CO_3^{2-} promoted early Mc intercalation nucleation [42]. At 28 d, these metastable phases disintegrated, reconstructing the CO_3^{2-} state.

3.4 Thermal decomposition behavior of the hydration products

To quantitatively evaluate the thermochemical stability of the hydration products and clarify the occurrence state of bound water and the thermal decomposition evolution mechanism of the carbonate phase in the matrix, TG-DTG was used to test and analyze the thermogravimetric loss of the optimal group (NH-4-2) of paste test blocks at different hydration ages.

The results are shown in Fig. 10. In the low-temperature range of 30 ~ 200°C (which corresponds mainly to the removal of interlayer water and physical adsorption water of (N) C- (A) -S-H gel), the weight loss of the system did not increase monotonically with increasing age but showed an abnormal trend of 7 d (3.82%) > 28 d (3.15%) > 3 d (2.80%). This phenomenon does not mean the stagnation of the hydration process but is determined by the intrinsic hydration kinetic evolution of the hybrid alkali-activated system.

Unlike traditional Portland cement, the water in the strong alkali excitation system mainly acts as a reaction medium rather than a skeleton component [44]. In the early stage of hydration (7 d), the structure of the primary (N) C- (A)-S-H gel is

relatively loose, and a large amount of physically adsorbed water and interlayer water are fixed during the formation of the early metastable phase. However, by the age of 28 d, the aluminosilicate skeleton has been relatively densified, and the water originally stored in the gel network is repelled into the capillary pores (converted into free water). Moreover, the crystalline water released by the disintegration of the metastable phase is superimposed[43], and a large amount of water is converted into a free state. Owing to this part of the free water in the TG test before the 40°C low-temperature predrying sample preparation stage, volatile loss occurred in advance, eventually leading to 28 d of sample measurement in the instrument, at which time the absolute low-temperature bound water content clearly decreased.

At 600–700°C ($CaCO_3$ decomposition), decarburization decreased from 4.827% (3 d) to 0.561% (28 d). This confirms calcite dissolution. Released CO_3^{2-} was encapsulated or intercalated into the 3D (N)C-(A)-S-H network. This increased its thermal decomposition barrier, reducing high-temperature weight loss.

3.5 Micromorphology analysis of the hydration products

To intuitively characterize the microstructure evolution of the hydration products and clarify the synergistic hydration mechanism of the multisource solid waste, the microstructures and element spatial distributions of the samples at different hydration ages were observed by SEM—EDS (Fig. 12).

At the early stage of hydration (7 d), a flocculent amorphous (N) C- (A)-S-H gel network initially formed in the system (Fig. 11a). Owing to the spatial extrusion of the rapid growth of the gel, the crystals that precipitated locally in the matrix failed to develop a regular geometric shape. These flaky and hexagonal plate-like crystals and amorphous gels undergo significant physical interweaving and wrapping (Fig. 11b). A typical crystal-gel interweaving region within the hardened matrix is shown in Fig. 11c. Hexagonal plate-like crystals that developed in the center of this region exhibit morphological features highly consistent with those of hydrotalcite-like (Ht) compounds and monocarbonate (Mc). Furthermore, EDS point scanning confirms the stable presence of Mg, directly validating the local nucleation of the Ht phase. Since pure layered Ht and Mc crystals do not contain Si, the detection of Si and Na signals indicates that the electron beam penetrated the surface crystals, exciting the underlying (N)C-(A)-S-H hybrid gel network. Considering that the isomorphous substitution of Al within the aluminosilicate gel network is strictly constrained by a structural saturation limit[45], a significant amount of excess free Al remains in this microregion. Driven by the local high abundance of free Ca^{2+} and CO_3^{2-}, this excess Al is highly prone to cross-linking with these free ions, which strongly implies the synergistic precipitation of Mc and other carbon-containing metastable crystalline phases.

Driven by the highly alkaline environment, the dissolution and exfoliation of the precursor particle surfaces persisted throughout the entire hydration process. By 28 d, profound dissolution features could be clearly observed (Fig. 11d). These roughened interfaces provided excellent heterogeneous nucleation sites, facilitating the firm attachment and outward extension of newly formed gels onto the unreacted particles, thereby significantly driving the densification of the matrix (Fig. 11e). Simultaneously, the initially loose gel network gradually evolved into highly dense gel clusters through continuous polycondensations, effectively filling interfacial capillary pores and structural defects.

Furthermore, EDS elemental mapping reveals a uniform and highly congruent spatial distribution of core elements (Ca, Si, Al, and O) within the dense matrix, indicating the full maturation of a stable three-dimensional hydration skeleton. Additionally, the diffuse distribution of endogenous S confirms that the tightly interlocked gel network effectively achieved deep physical encapsulation and microscale immobilization of potentially harmful ions, such as SO_4^{2-}, within the system (Fig. 11f).

3.6 Leaching toxicity test

Figure 12 illustrates the leaching concentrations of EMR, Ref (28d), and NH-4-2 (28d). The raw EMR presents severe environmental risks. Its leaching concentrations of Mn, NH_4^+-N, and SO_4^{2-} reach 683370 μg/L, 366000 μg/L, and 5571000 μg/L, respectively. These values far exceed the standard limits.

After solidification, the Mn concentrations in both the Ref and NH-4-2 groups drop to below 3.6 μg/L. This value strictly complies with the GB/T 14848 – 2024 (Class III) limit (100 μg/L). The SO_4^{2-} concentrations decrease to 122000 μg/L for the Ref group and 69000 μg/L for the NH-4-2 group. Both are safely below the 250000 μg/L threshold. This massive reduction confirms the efficient physical encapsulation provided by the dense (N)C-(A)-S-H gel. It also proves the successful chemical fixation of sulfates during the phase reconstruction process. The NH_4^+-N leaching behavior strictly highlights the necessity of the hybrid alkali activation design. The Ref group reduces the NH_4^+-N concentration to 3070 μg/L. However, this value still fails to meet the regulatory limit (500 μg/L). The initial ternary precursor without strong alkali excitation cannot sufficiently seal highly mobile nitrogen.

In contrast, the optimal NH-4-2 group successfully reduces the NH_4^+-N leaching concentration to 407 μg/L. This compliance relies on two synergistic factors. First, the initial alkaline deammoniation pretreatment removes the majority of the free ammonia. Second, the highly polymerized hybrid matrix tightly seals the residual ammonium ions within its three-dimensional cross-linked network.

These results prove that the NH-4-2 hybrid system successfully neutralizes the leaching risks of multi-source solid wastes. The prepared material meets the stringent environmental safety requirements for underground mine backfilling operations.

4 Conclusion

In this study, on the basis of granulated blast furnace slag (GGBS), electrolytic manganese slag (EMR) and lead-zinc tailings (LZMT), a low-carbon and environmentally friendly hybrid alkali-activated ternary solid waste-based cementitious material was developed. The following conclusions are drawn:

1. An optimal skeleton ratio is established for the D-optimal design. In the absence of an external alkali, LZMT acted solely as an inert physical filler and heterogeneous nucleation site. Moreover, EMR provided sulfate excitation, and GGBS constructed the basic gel network.
2. An activator (4% Na_2O equivalent, *Ms* = 1.5 NaOH and Na_2SiO_3) with 10% cement yielded optimal performance. The initial/final setting times were 55/115 min. The 28 d strength reached 43 MPa. Reducing the amount of cement decreased the Ca^{2+} concentration, preventing flash setting and the common-ion effect.
3. With external alkali excitation, the role of the LZMT fundamentally changed. It transitioned from an inert filler to a chemically active component. The strongly alkaline environment drove surface dissolution. The released CO_3^{2-} promoted the early (7 d) formation of metastable Mc and Ht phases, serving as a microcrystalline skeleton. Over time, the metastable phases transformed into highly polymerized amorphous (N)C-(A)-S-H gels. This dense 3D skeleton achieved effective physical encapsulation of endogenous SO_4^{2-}.
4. The optimal hybrid matrix demonstrated outstanding environmental safety. Through synergistic chemical bonding and physical encapsulation, the leaching concentrations of characteristic pollutants (Mn, NH_4^+-N, and SO_4^{2-}) were drastically reduced compared to raw EMR. All leaching indicators successfully met the strict Class III limits of the Groundwater Quality Standard (GB/T 14848 – 2024).
5. Methodologically, the two-step optimization strategy independently evaluated the alkali excitation effect. However, strong alkalis alter precursor depolymerization and phase equilibria. Therefore, the optimal skeleton ratio derived without external alkali may deviate slightly from the absolute optimum. The development of a comprehensive global optimization model that incorporates activator parameters will be the focus of our future work.

Declarations

Competing Interests

The authors have no relevant financial or non-financial interests to disclose.

Data Availability

The datasets generated during and/or analysed during the current study are available from the corresponding author on reasonable request.

Funding:

The authors declare that no funds, grants, or other support were received during the preparation of this manuscript.

Author Contributions:

Ziyu Zou: Conceptualization, Methodology, Investigation, Formal analysis & Writing – original draft. **Zecheng Zeng**: Investigation, Data curation & Formal analysis. **Mengqi Zeng**: Validation, Writing – review & editing. **Zhenjun Wu**: Conceptualization, Supervision, Resources, Writing – review & editing. All authors commented on previous versions of the manuscript. All authors read and approved the final manuscript.

References

1. Lothenbach, B., Scrivener, K., Hooton, R.D.: Supplementary cementitious materials. Cem. Concr. Res. **41**, 1244–1256 (2011). https://doi.org/10.1016/j.cemconres.2010.12.001
2. Johansson, L., Bahrami, A., Cehlin, M., Wallhagen, M.: Experimental Investigation on Using Lead–Zinc Tailings as Low-Carbon Partial Replacement of Cement in Mortar for Sustainable Construction. Buildings. **16**, 730 (2026). https://doi.org/10.3390/buildings16040730
3. Fu, Y., Qiao, H., Feng, Q., Chen, K., Li, Y., Jia, Z., Xue, C.: Impact of desulphurized electrolytic manganese residue-assisted cementitious materials on silicate cement hydration and environmental safety assessment. J. Building Eng. **94**, 109906 (2024). https://doi.org/10.1016/j.jobe.2024.109906
4. Nie, X., Lang, L., Liu, L., Li, J., Long, S.: Development of low-carbon cementitious materials utilizing electrolytic manganese residue and industrial solid wastes: Environmental performance and strength mechanisms. Sustainable Chem. Pharm. **43**, 101916 (2025). https://doi.org/10.1016/j.scp.2025.101916
5. Tian, J., Liu, W., Yin, H., Chu, Q., Lv, Z., Nie, W.: Study on the mechanical properties and environmental characteristics of the new electrolytic manganese residue-based all-solid waste filling material. J. Environ. Chem. Eng. **13**, 119449 (2025). https://doi.org/10.1016/j.jece.2025.119449
6. Tang, L., He, Z., Pei, S., Han, J., Zou, M., Qin, M., Yu, Z.: Hydration characteristics and pollutant solidification mechanism of full solid waste electrolytic manganese residue super sulfate cement. J. Building Eng. **84**, 108563 (2024). https://doi.org/10.1016/j.jobe.2024.108563
7. Wang, J., Peng, B., Chai, L., Zhang, Q., Liu, Q.: Preparation of electrolytic manganese residue–ground granulated blastfurnace slag cement. Powder Technol. **241**, 12–18 (2013). https://doi.org/10.1016/j.powtec.2013.03.003
8. Wang, F., Long, G., Bai, M., Shi, Y., Zhou, J.L.: Feasibility of low-carbon electrolytic manganese residue-based supplementary cementitious materials. Sci. Total Environ. **883**, 163672 (2023). https://doi.org/10.1016/j.scitotenv.2023.163672
9. Xu, Y., Liu, X., Zhang, Y., Tang, B., Mukiza, E.: Investigation on sulfate activation of electrolytic manganese residue on early activity of blast furnace slag in cement-based cementitious material. Constr. Build. Mater. **229**, 116831 (2019). https://doi.org/10.1016/j.conbuildmat.2019.116831
10. Xuexian, J., Lusen, W., Weiguang, Z., Zhonglin, L., Yibing, L.: Synergistic mechanism of electrolytic manganese residue and red mud in ground granulated blast furnace slag -based cementitious materials system: Multiscale analysis based

on hydration characteristics and mechanical properties. Case Stud. Constr. Mater. **23**, e05320 (2025). https://doi.org/10.1016/j.cscm.2025.e05320

11. Li, J., Liu, Y., Ke, X., Jiao, X., Li, R., Shi, C.: Geopolymer synthesized from electrolytic manganese residue and lead-zinc smelting slag: Compressive strength and heavy metal immobilization. Cem. Concr. Compos. **134**, 104806 (2022). https://doi.org/10.1016/j.cemconcomp.2022.104806
12. Mi, B., Zhao, H., Lu, M., Zhou, Y., Xue, Y.: Synthesis of Electrolytic Manganese Slag–Solid Waste-Based Geopolymers: Compressive Strength and Mn Immobilization. Mater. (Basel). **17**, 1431 (2024). https://doi.org/10.3390/ma17061431
13. Tang, L., He, Z., Mi, T., Xiong, Q., Liu, Q., Zhi, Y., Xian, X.: Sustainable utilization of electrolytic manganese residue in cement-free binders: Strength mechanism, microstructure, hydration behavior and environmental performance. Chem. Eng. J. **535**, 175132 (2026). https://doi.org/10.1016/j.cej.2026.175132
14. Giretti, D., Fioravante, V., Been, K., Dickenson, S.: Mechanical properties of a carbonate sand from a dredged hydraulic fill. Géotechnique. **68**, 410–420 (2018). https://doi.org/10.1680/jgeot.16.P.304
15. Hu, Y., Yin, S., Li, K., Han, B., Zhang, B.: Formation mechanism and thermal decomposition properties of hydration products of superfine tailings cemented paste backfill. Arab. J. Chem. **16**, 104977 (2023). https://doi.org/10.1016/j.arabjc.2023.104977
16. Cui, W., Liu, J., Duan, W., Xie, M., Li, X., Dong, X.: Study on the synergistic effects and eco-friendly performance of red mud-based quaternary cementitious materials. Constr. Build. Mater. **428**, 136352 (2024). https://doi.org/10.1016/j.conbuildmat.2024.136352
17. Fu, Y., Xu, Z., Zhang, X., Lu, Q., Sun, Z., Wang, X.: Synthesis and Performance Evaluation of Nano-Calcium Carbonate-Modified Geopolymers Incorporating Fly Ash and Manganese Slag: A Comprehensive Investigative Study. Processes. **11**, 3418 (2023). https://doi.org/10.3390/pr11123418
18. Wu, Y., Sun, A., Huang, H., Wang, C., Barbarulo, R., Zhang, Q., Uppalapati, S., Wang, B.: Preparation and performance optimization of ternary cements containing calcined coal gangue and limestone. Constr. Build. Mater. **493**, 143303 (2025). https://doi.org/10.1016/j.conbuildmat.2025.143303
19. Matschei, T., Lothenbach, B., Glasser, F.P.: The role of calcium carbonate in cement hydration. Cem. Concr. Res. **37**, 551–558 (2007). https://doi.org/10.1016/j.cemconres.2006.10.013
20. Scrivener, K., Martirena, F., Bishnoi, S., Maity, S.: Calcined clay limestone cements (LC3). Cement and Concrete Research. **114**, 49–56 (2018). https://doi.org/10.1016/j.cemconres.2017.08.017
21. Hameed, R., Seo, J., Park, S., Amr, I.T., Lee, H.K.: CO_2 Uptake and Physicochemical Properties of Carbonation-Cured Ternary Blend Portland Cement–Metakaolin–Limestone Pastes. Materials. **13** (2020). https://doi.org/10.3390/ma13204656
22. Vázquez-Rodríguez, F., Elizondo, N., Montes-González, M., Gómez-Rodríguez, C., González-Carranza, Y., Guzmán, A.M., Rodríguez, E.A.: Microstructural and Mechanical Characteristics of Alkali-Activated Binders Composed of Milled Fly Ash and Granulated Blast Furnace Slag with μ-Limestone Addition. Materials. **16** (2023). https://doi.org/10.3390/ma16103818
23. Wardhono, A.: The effect of water binder ratio on strength development of class C fly ash geopolymer mortar prepared by dry geopolymer powder. MATEC Web Conf. **258**, 05032 (2019). https://doi.org/10.1051/matecconf/201925805032
24. Jia, Z.: The Impact of Calcined Electrolytic Manganese Residue on the Sulfate Resistance of Cement-Based Materials. E3S Web Conf. **618**, 02007 (2025). https://doi.org/10.1051/e3sconf/202561802007
25. Chen, S., Wang, F., Ma, L., Che, J.: Study on Physical Properties of Desulfurized Electrolytic Manganese Residue Cement and Properties of Mortar. Materials. **16**, 4035 (2023). https://doi.org/10.3390/ma16114035
26. Wang, Y., Zhang, N., Ren, Y., Xu, Y., Liu, X.: Effect of Electrolytic Manganese Residue in Fly Ash-Based Cementitious Material: Hydration Behavior and Microstructure. Materials. **14**, 7047 (2021). https://doi.org/10.3390/ma14227047

27. Tian, Y., Yang, C., Yuan, S., Yuan, H., Yang, K., Yu, L., Zhang, M., Zhu, X.: Understanding the rheological properties of alkali-activated slag pastes from the cohesion and friction interactions. Constr. Build. Mater. **291**, 123311 (2021). https://doi.org/10.1016/j.conbuildmat.2021.123311
28. Puertas, F., Varga, C., Alonso, M.M.: Rheology of alkali-activated slag pastes. Effect of the nature and concentration of the activating solution. Cem. Concr. Compos. **53**, 279–288 (2014). https://doi.org/10.1016/j.cemconcomp.2014.07.012
29. Bernal, S.A., Nicolas, R.S., van Deventer, J.S.J., Provis, J.L.: Alkali-activated slag cements produced with a blended sodium carbonate/sodium silicate activator. Adv. Cem. Res. **28**, 262–273 (2015). https://doi.org/10.1680/jadcr.15.00013
30. Fernández-Jiménez, A., Puertas, F.: Effect of activator mix on the hydration and strength behaviour of alkali-activated slag cements. Adv. Cem. Res. **15**, 129–136 (2003). https://doi.org/10.1680/adcr.2003.15.3.129
31. Fernández-Jiménez, A., Puertas, F.: Alkali-activated slag cements: Kinetic studies. Cem. Concr. Res. **27**, 359–368 (1997). https://doi.org/10.1016/S0008-8846(97)00040-9
32. Ahmed, M.J., Lambrechts, K., Ling, X., Schollbach, K., Brouwers, H.J.H.: Effect of hydroxide, carbonate, and sulphate anions on the β-dicalcium silicate hydration rate. Cem. Concr. Res. **173**, 107302 (2023). https://doi.org/10.1016/j.cemconres.2023.107302
33. Kumar, A., Sant, G., Patapy, C., Gianocca, C., Scrivener, K.L.: The influence of sodium and potassium hydroxide on alite hydration: Experiments and simulations. Cem. Concr. Res. **42**, 1513–1523 (2012). https://doi.org/10.1016/j.cemconres.2012.07.003
34. Suwan, T., Fan, M.: Influence of OPC replacement and manufacturing procedures on the properties of self-cured geopolymer. Constr. Build. Mater. **73**, 551–561 (2014). https://doi.org/10.1016/j.conbuildmat.2014.09.065
35. Garcia-Lodeiro, I., Donatello, S., Fernández-Jiménez, A., Palomo, Á.: Hydration of Hybrid Alkaline Cement Containing a Very Large Proportion of Fly Ash: A Descriptive Model. Materials. **9**, 605 (2016). https://doi.org/10.3390/ma9070605
36. Zhu, X., Luan, M., Tang, D., Yang, K., Yang, C.: Understanding the setting behaviours of alkali-activated slag from the dissolution-precipitation point of view. Cem. Concr. Compos. **148**, 105474 (2024). https://doi.org/10.1016/j.cemconcomp.2024.105474
37. Dener, M., Karatas, M., Shi, J., Mohabbi, M.: Mechanical properties and microstructure of hybrid alkali-activated cement component. Arch. Civ. Mech. Eng. **25**, 45 (2024). https://doi.org/10.1007/s43452-024-01054-w
38. Zhou, Y., Zhan, Y., Gao, H., Zhu, R.: Early properties and reaction mechanism of hybrid alkali-activated cements (HAACs). Mater. Today Commun. **41**, 110849 (2024). https://doi.org/10.1016/j.mtcomm.2024.110849
39. Zhao, P., Lu, L., Liu, X., De la Torre, A.G., Cheng, X.: Error Analysis and Correction for Quantitative Phase Analysis Based on Rietveld-Internal Standard Method: Whether the Minor Phases Can Be Ignored? Crystals. 8, 110 (2018). https://doi.org/10.3390/cryst8030110
40. Barbarulo, R., Peycelon, H., Leclercq, S.: Chemical equilibria between C–S–H and ettringite, at 20 and 85°C. Cem. Concr. Res. **37**, 1176–1181 (2007). https://doi.org/10.1016/j.cemconres.2007.04.013
41. Richardson, I.G.: The nature of C-S-H in hardened cements. Cem. Concr. Res. **29**, 1131–1147 (1999). https://doi.org/10.1016/S0008-8846(99)00168-4
42. Ke, X., Bernal, S.A., Provis, J.L., Lothenbach, B.: Thermodynamic modelling of phase evolution in alkali-activated slag cements exposed to carbon dioxide. Cem. Concr. Res. **136**, 106158 (2020). https://doi.org/10.1016/j.cemconres.2020.106158
43. Myers, R.J., Lothenbach, B., Bernal, S.A., Provis, J.L.: Thermodynamic modelling of alkali-activated slag cements. Appl. Geochem. **61**, 233–247 (2015). https://doi.org/10.1016/j.apgeochem.2015.06.006
44. Duxson, P., Provis, J.L., Lukey, G.C., Mallicoat, S.W., Kriven, W.M., Van Deventer, J.S.J.: Understanding the relationship between geopolymer composition, microstructure and mechanical properties. Colloids Surf., A. **269**, 47–58 (2005).

https://doi.org/10.1016/j.colsurfa.2005.06.060

45. L'Hôpital, E., Lothenbach, B., Le Saout, G., Kulik, D., Scrivener, K.: Incorporation of aluminium in calcium-silicate-hydrates. Cem. Concr. Res. **75**, 91–103 (2015). https://doi.org/10.1016/j.cemconres.2015.04.007

Figures

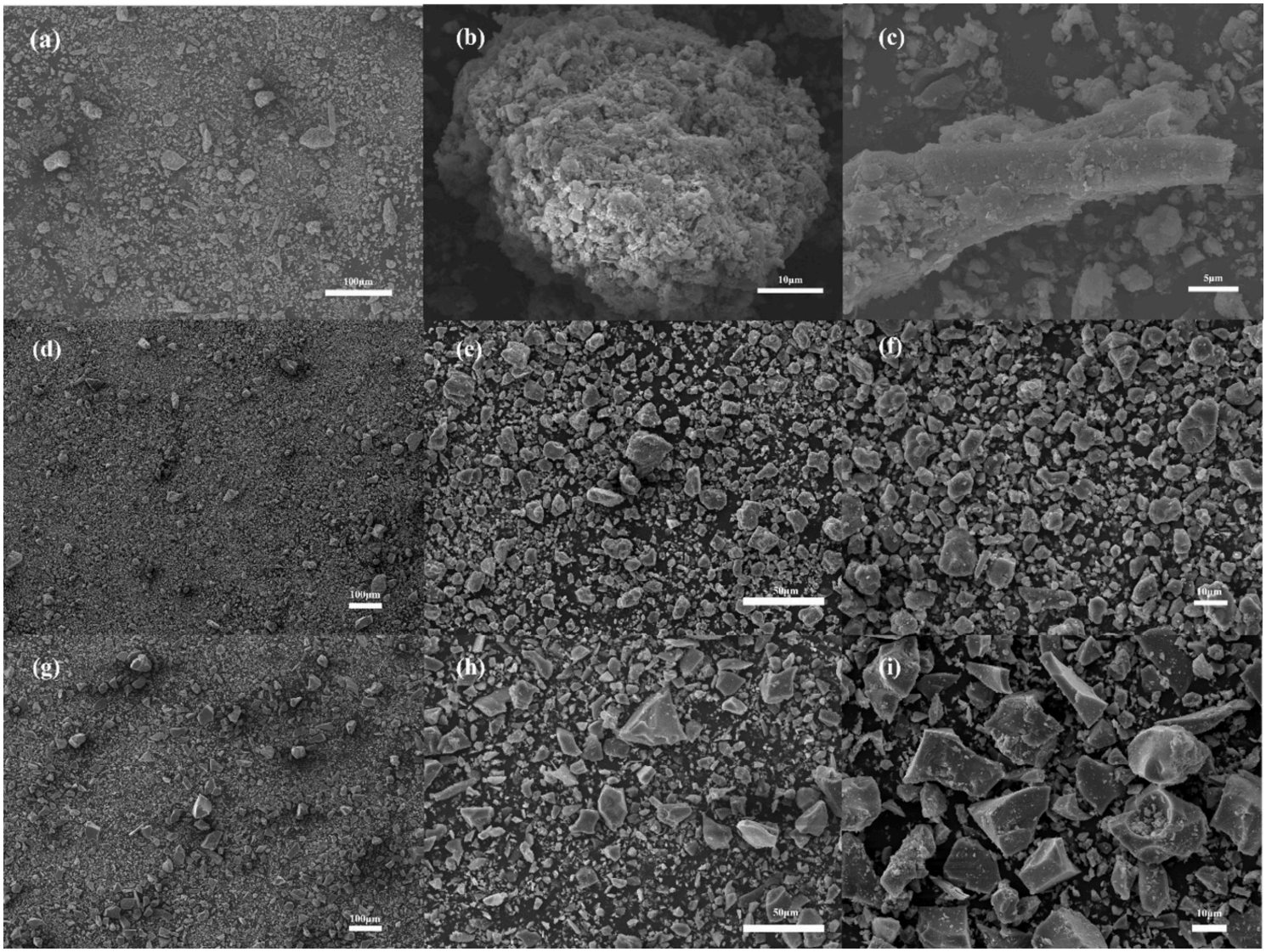


Figure 1

SEM images of each raw material: (a-c) EMR, (d-f) LZMT, (g-i) GGBS

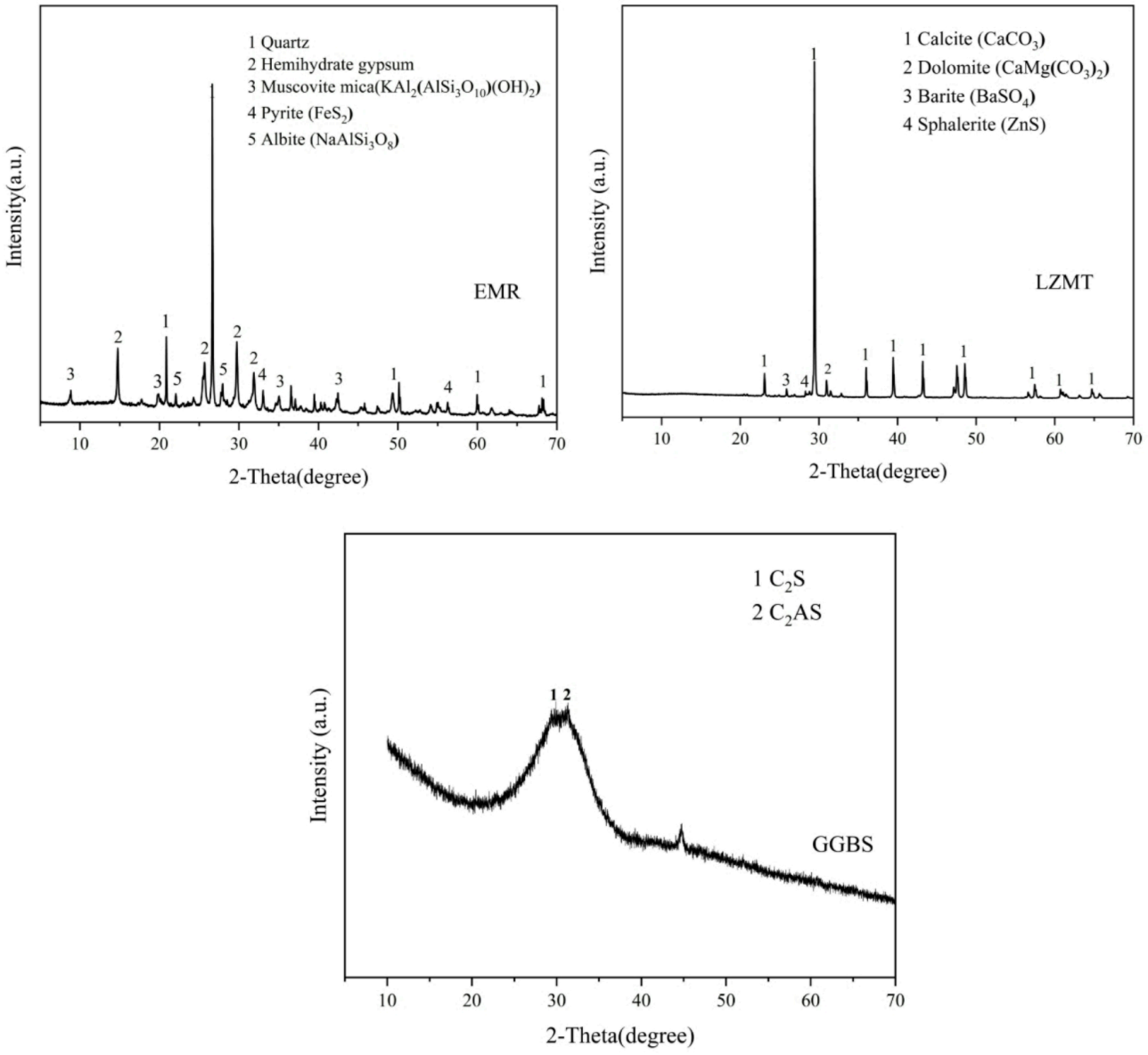


Figure 2

X-ray diffraction pattern of each raw material

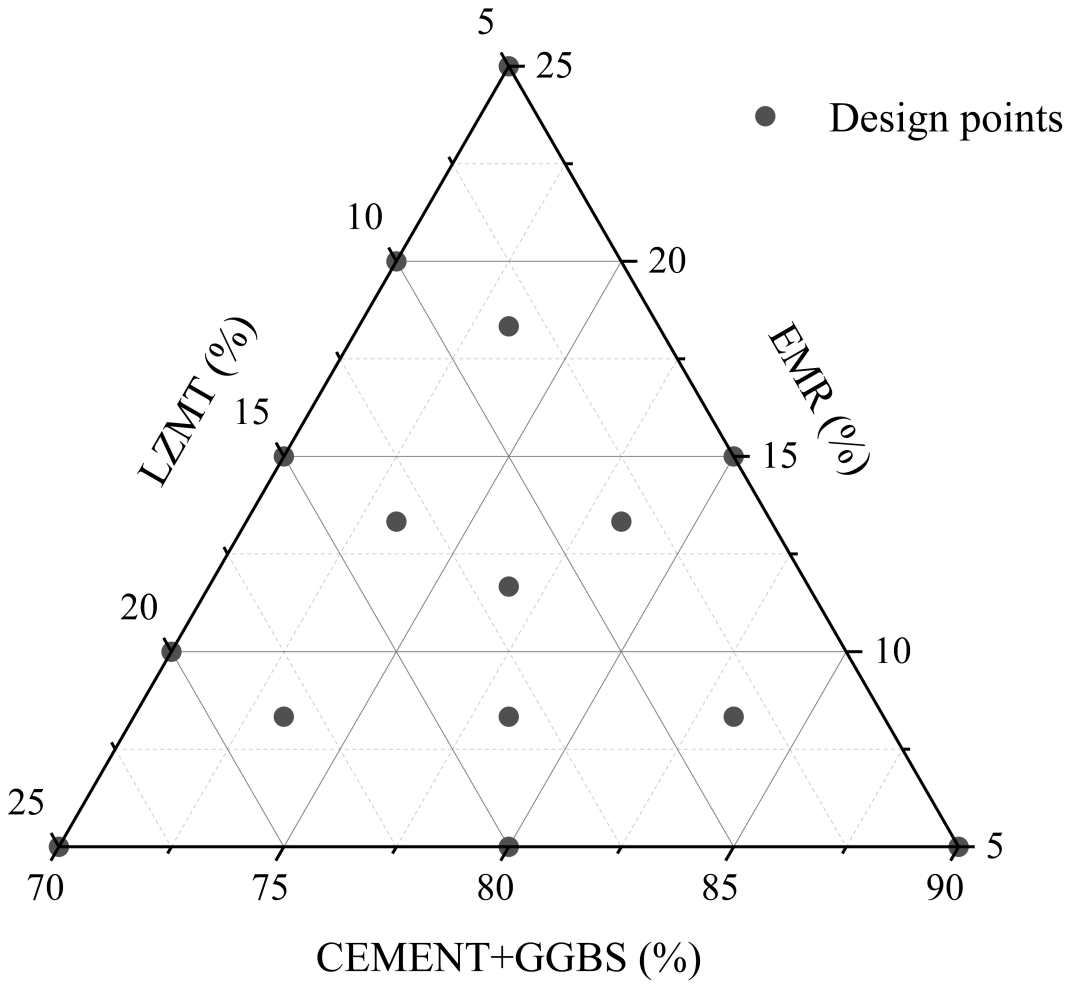


Figure 3

Distribution of design points in the D-optimal mixture design

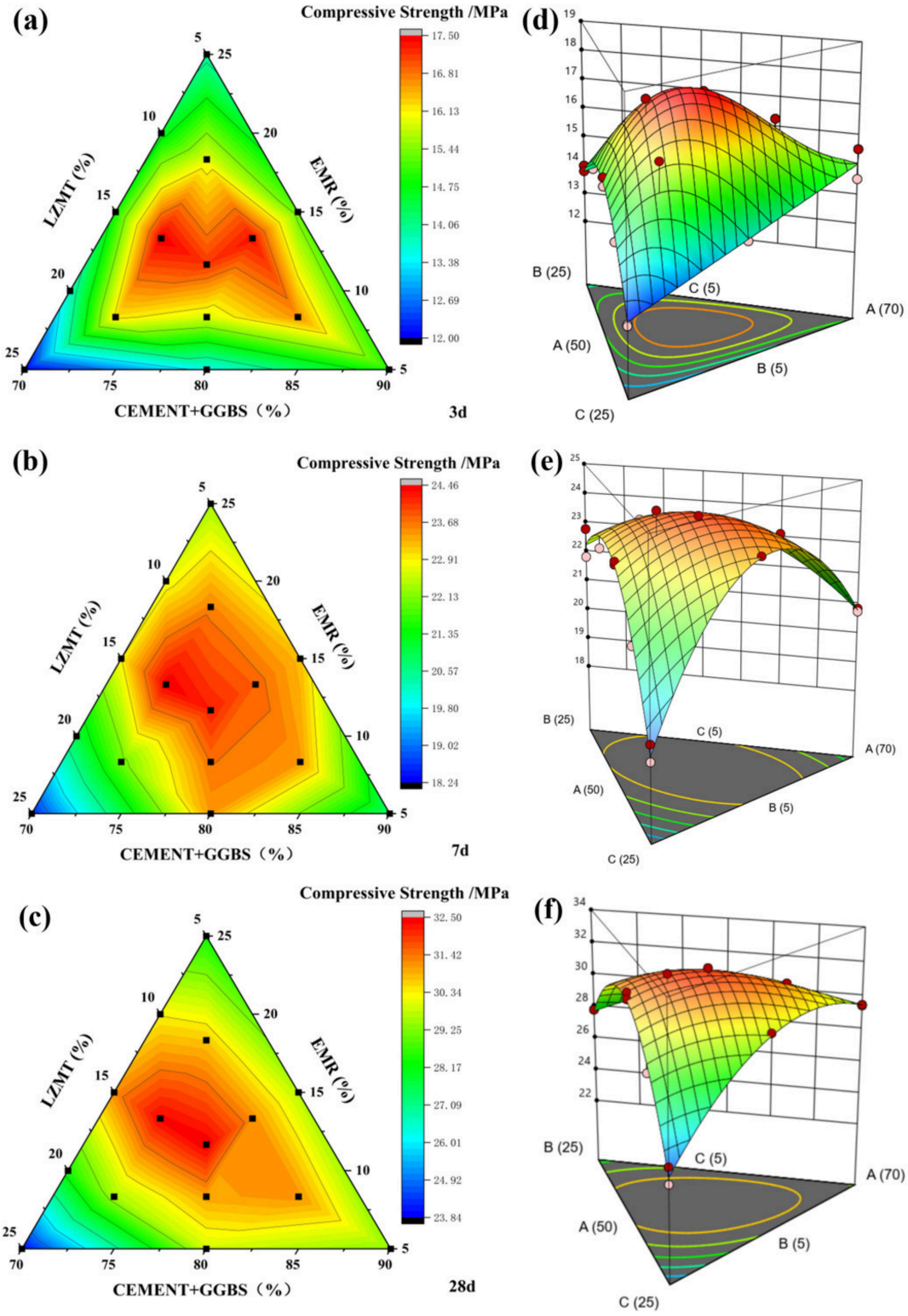


Figure 4

The compressive strength of each group of mortar: (a–c) compressive strength distribution; (d–f) 3 d surface figure of compressive strength based on Design Expert software.

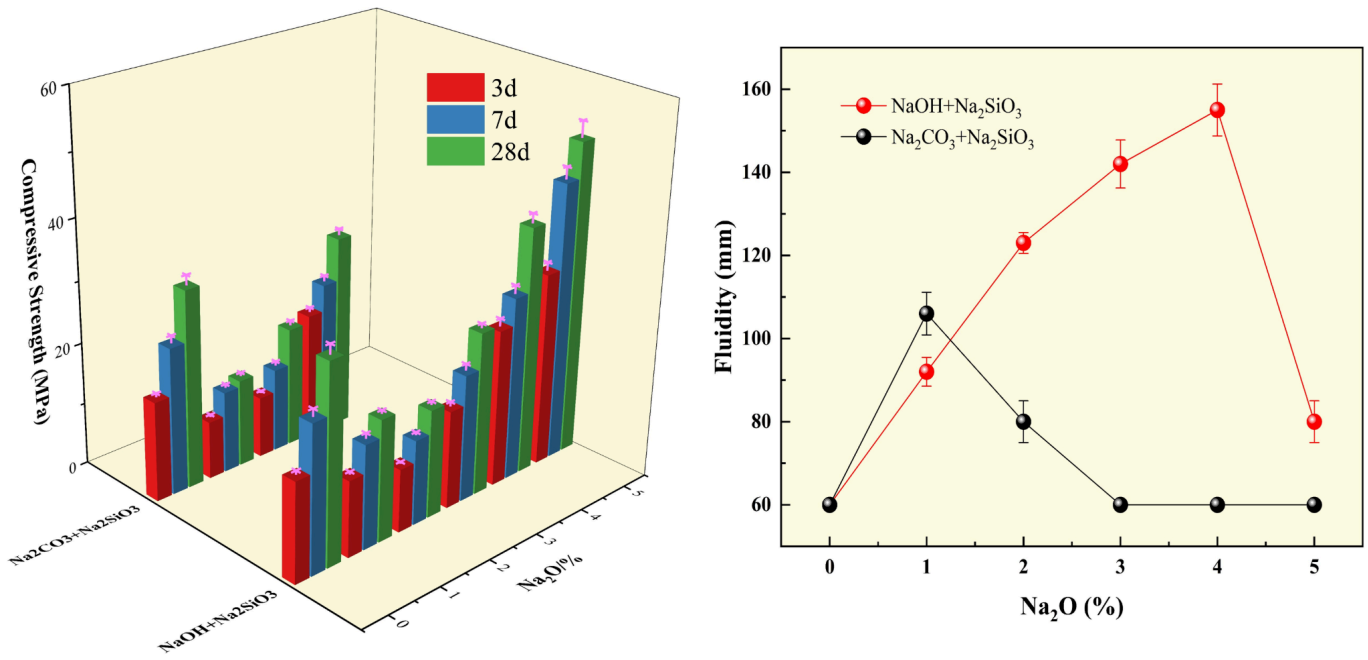


Figure 5

(a) Effect of the type/content of the alkali activator on the compressive strength; (b) effect of the type/content of the alkali activator on expansion. Error bars represent the standard deviation of three parallel samples.

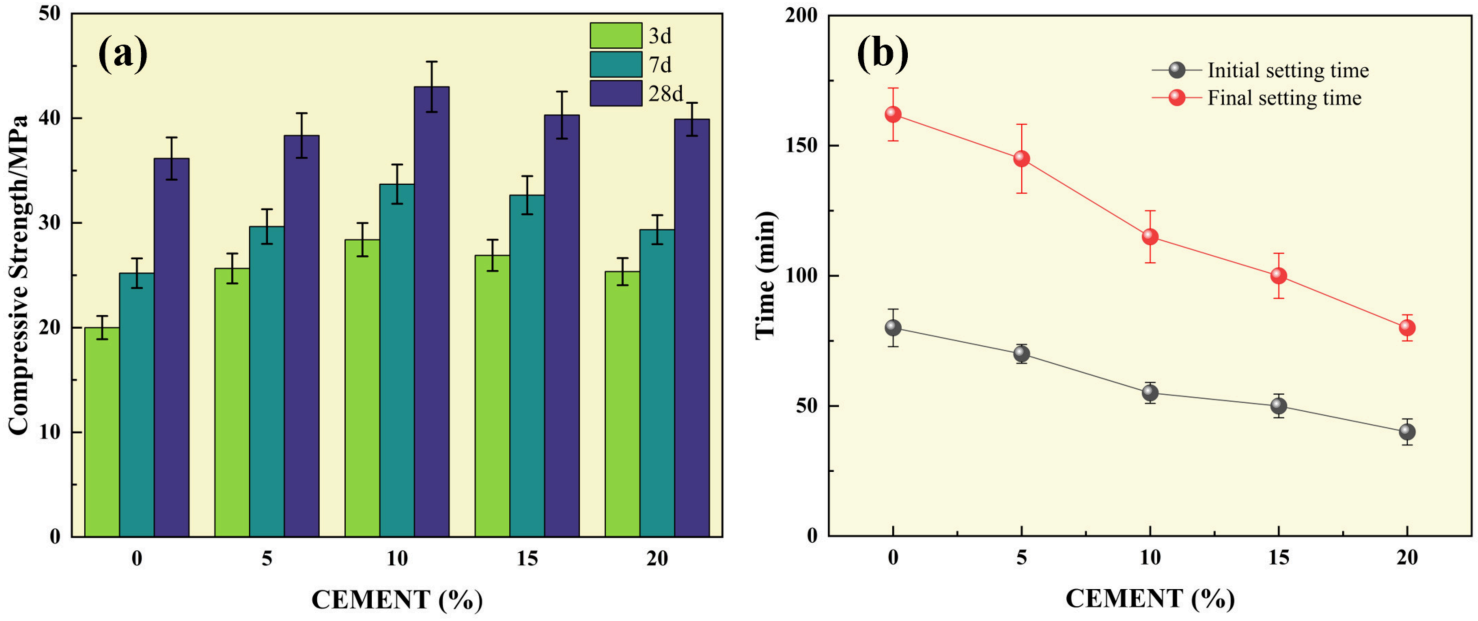


Figure 6

Effect of OPC content on the (a) compressive strength and (b) setting times of the NH-4 system. Error bars represent the standard deviation of three parallel samples.

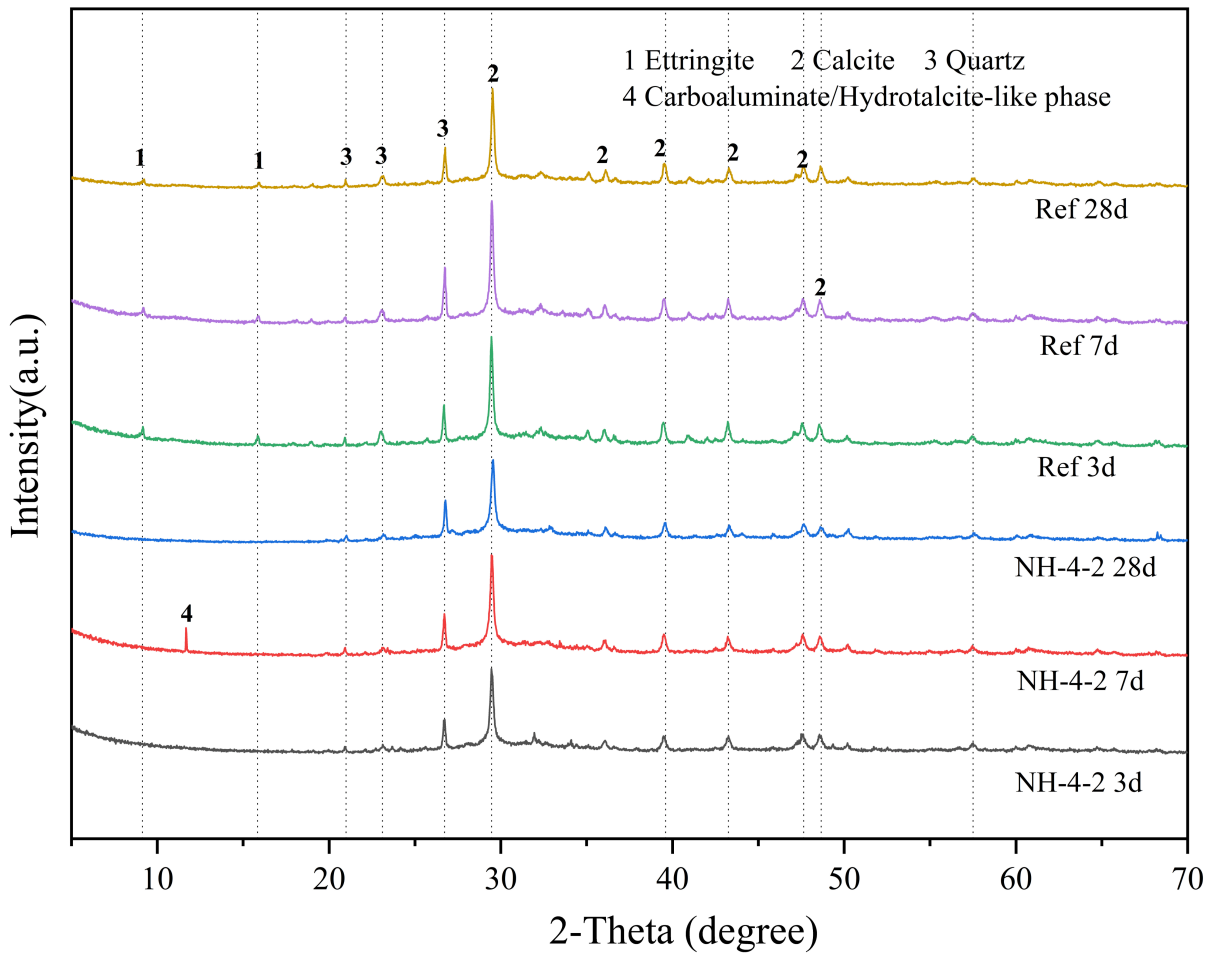


Figure 7

X-ray diffraction patterns of the Ref group and the NH-4-2 group at different ages

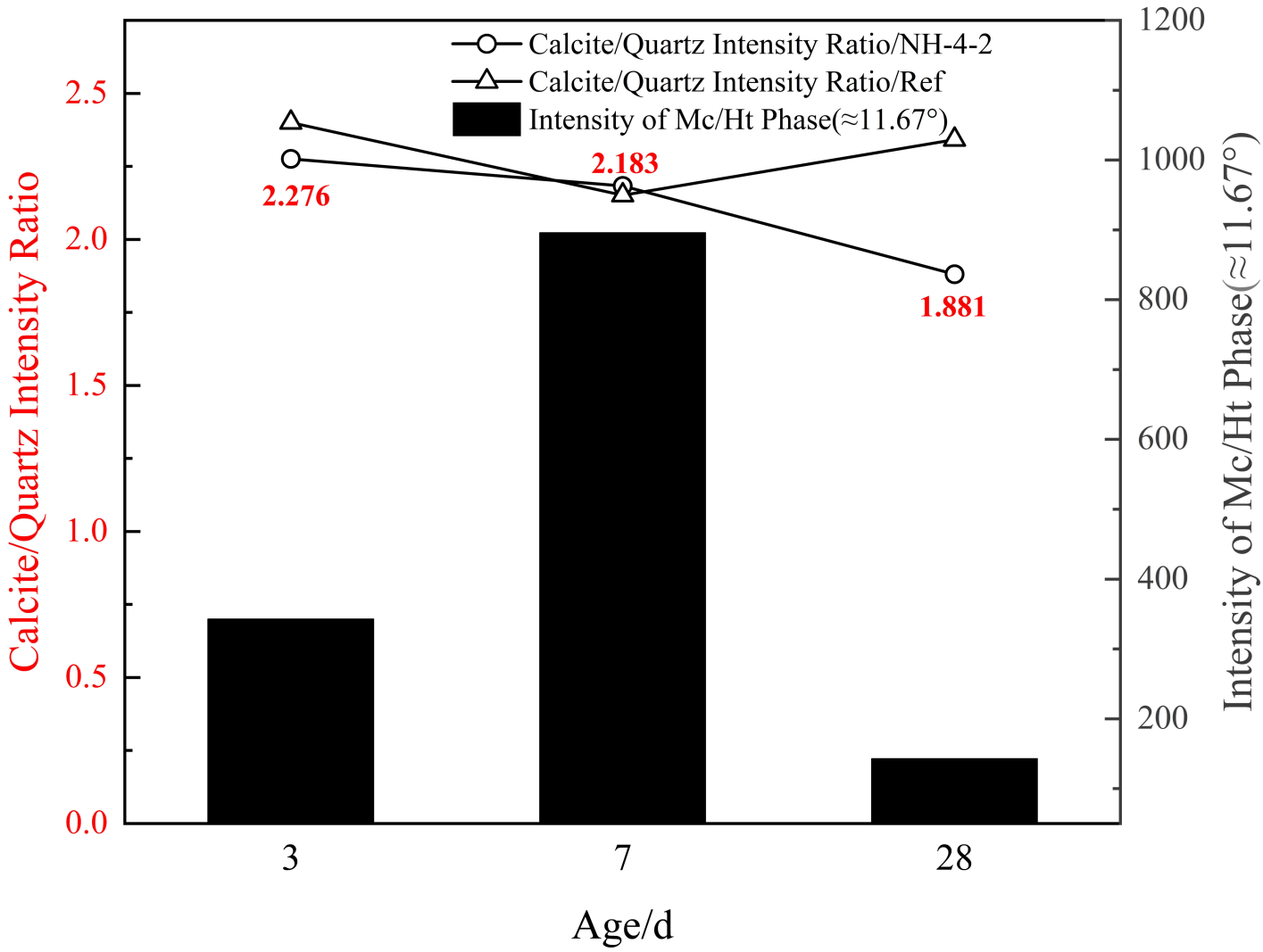


Figure 8

Relative abundance of calcite and evolution of the Mc/Ht phase diffraction intensity with age based on the internal standard method (calcite/quartz)

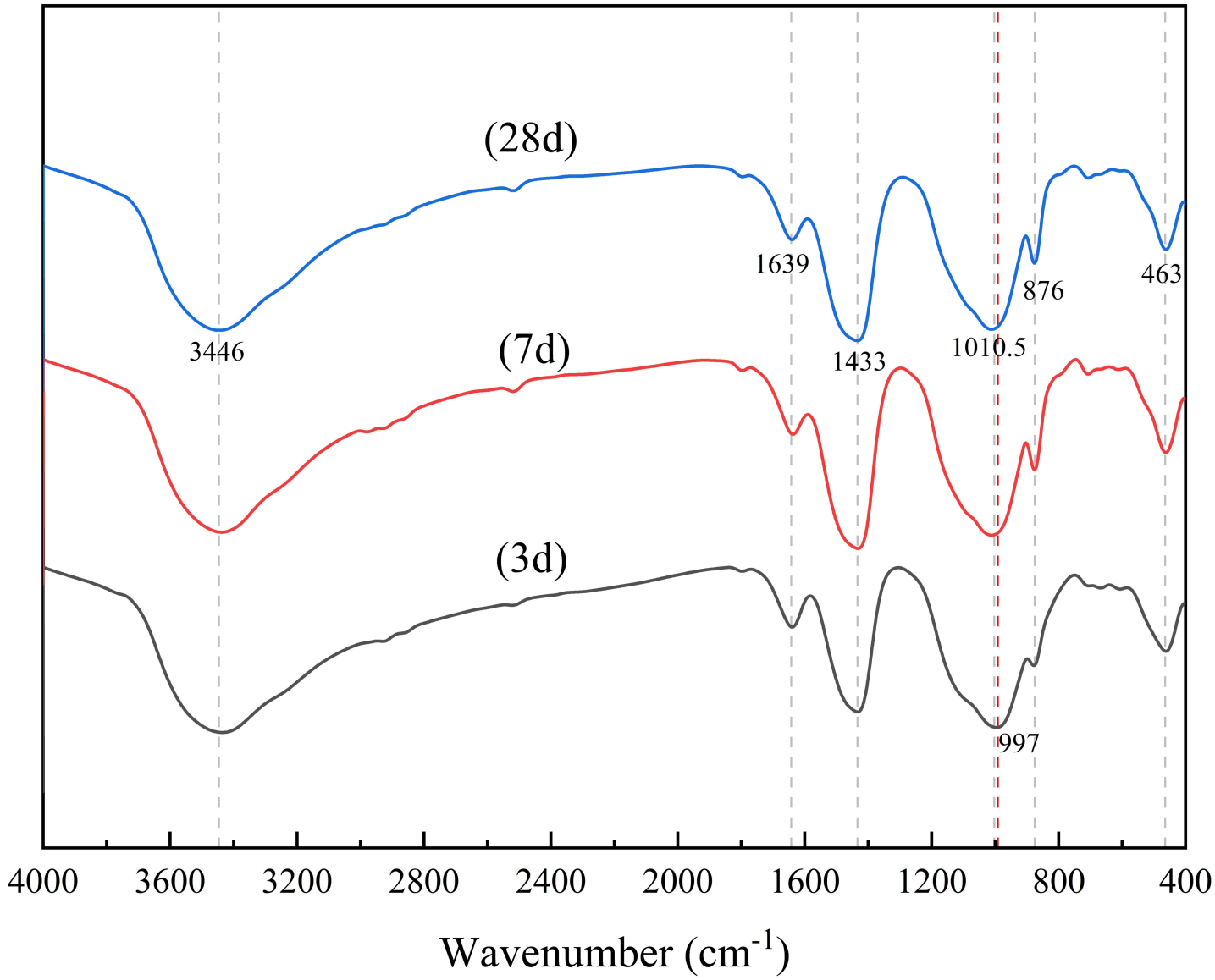


Figure 9

FTIR spectra of the hydration products for different ages of the NH-4-2 group

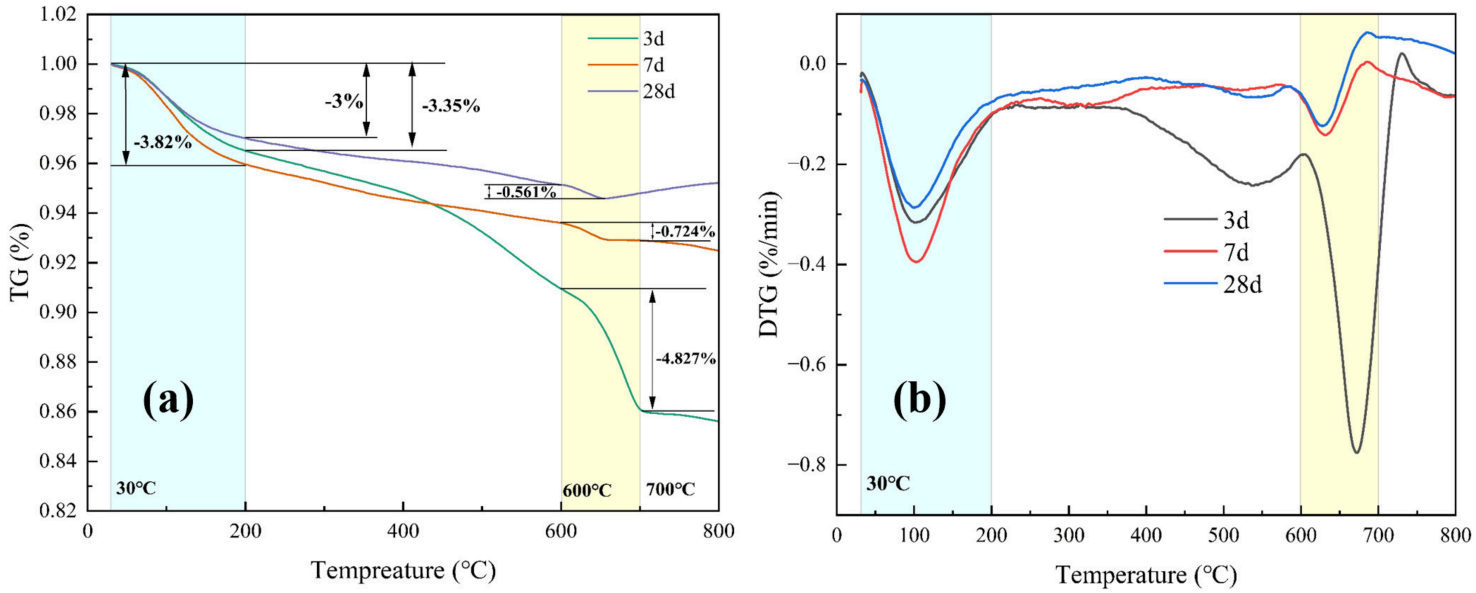


Figure 10

TG curve (a) and DTG curve (b) of NH-4-2 paste test blocks at different ages.

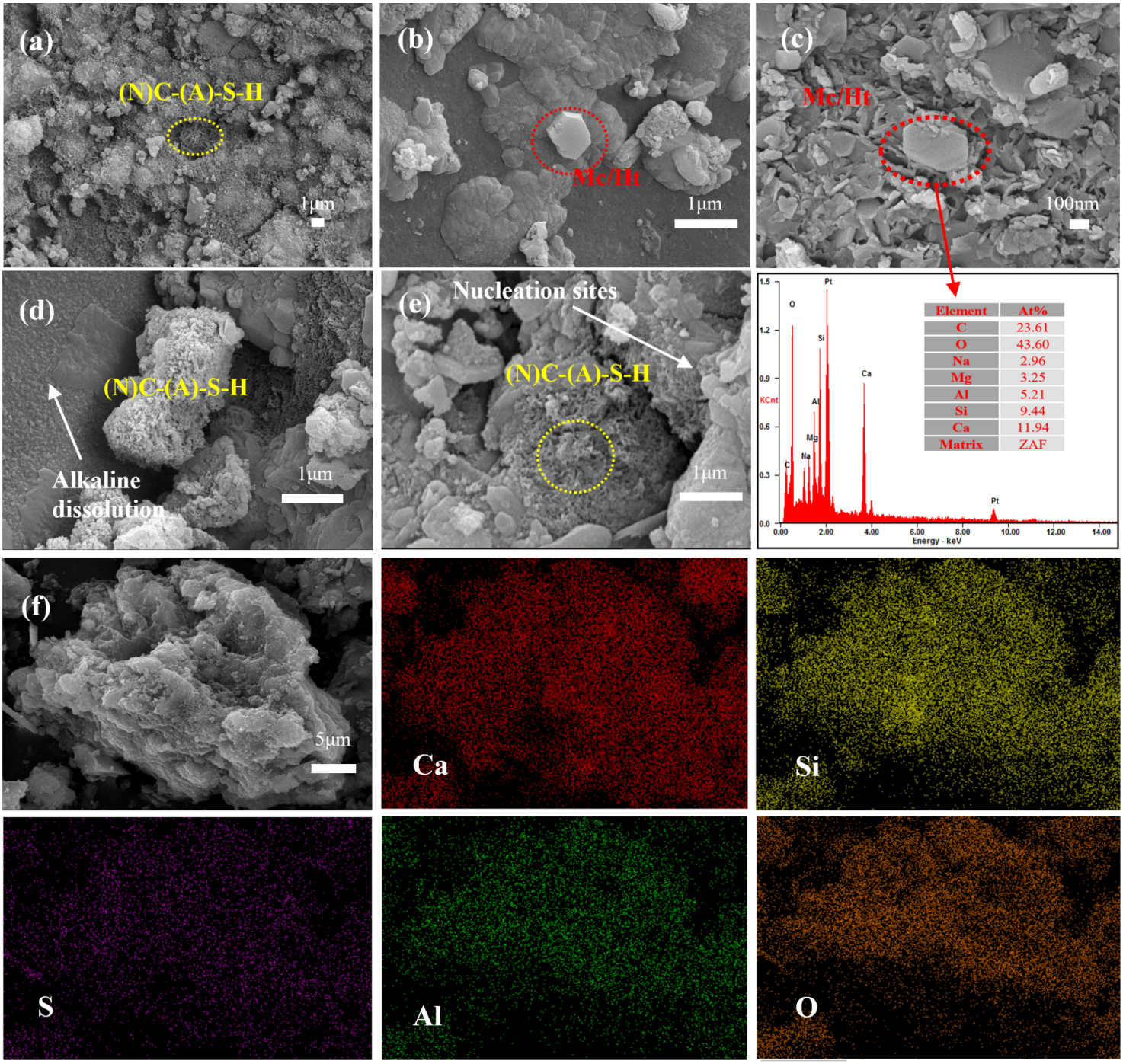


Figure 11

Microstructure and energy spectrum analysis of solidified bodies filled at different hydration ages: (a) 7 d: flocculent (N) C-(A) -S-H gel network; (b) 7 d: Mc/Ht composite intercalation phase embedded in the gel; (c) 7 d: typical hexagonal lamellar intercalation phase and its corresponding EDS point scanning energy spectrum; (d, e) 28 d: alkaline corrosion on the surface of the precursor, heterogeneous nucleation sites and further densification of the gel; (f) 28 d: highly condensed gel clusters and their corresponding EDS element surface scanning distribution.

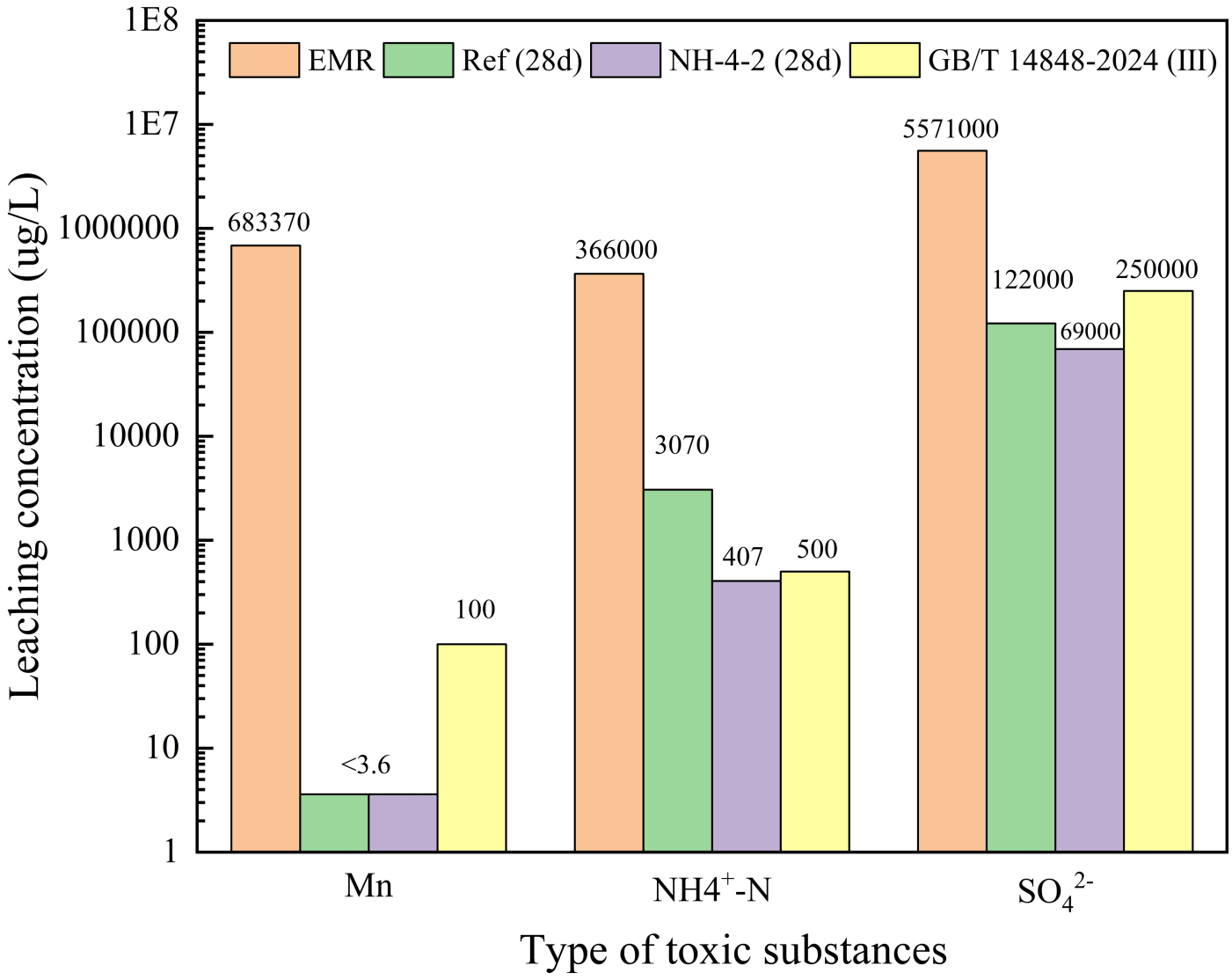


Figure 12

Comparison of leaching concentrations before and after solidification.

Supplementary Files

This is a list of supplementary files associated with this preprint. Click to download.

- floatimage1.jpeg